

Reactivity of chondritic meteorites under H₂-rich atmospheres: Formation of H₂S.

V. Cabedo,^{1*} G. Pareras,² J. Allitt,¹ A. Rimola,² J. Llorca,³ H. H. P. Yiu,¹ M. R. S. McCoustra¹

¹*Institute of Chemical Sciences, Heriot-Watt University, Edinburgh, EH14 4AS, Scotland.*

²*Departament de Química, Universitat Autònoma de Barcelona, 08193 Bellaterra, Catalonia, Spain.*

³*Institut de Tècniques Energètiques, Departament d'Enginyeria Química, Universitat Politècnica de Catalunya, Barcelona, Catalonia, Spain.*

Accepted XXX. Received YYY; in original form ZZZ

ABSTRACT

Current models of chemical evolution during star and planetary formation rely on the presence of dust grains to act as a third body. However, they generally ignore the reactivity of the dust grains themselves. Dust grains present in the protoplanetary phase will evolve as the solar system forms and, after protoplanets have appeared, they will be constantly delivered to their surfaces in the form of large aggregates or meteorites. Chondritic meteorites are mostly unaltered samples of the dust present in the first stages of the Solar System formation, that still arrive nowadays to the surface of Earth and allow us to study the properties of the materials forming the early Solar System. These materials contain, amongst others, transition metals that can potentially act as catalysts, as well as other phases that can potentially react in different astrophysical conditions, such as FeS. In this work, we present the reactivity of chondritic meteorites under H₂-rich atmospheres, particularly towards the reduction of FeS for the formation of H₂S and metallic Fe during the early phases of the planetary formation. We present the obtained results on the reaction rates and the percentage of FeS available to react in the materials. Additionally, we include a computational study of the reaction mechanism and the energetics. Finally, we discuss the implications of an early formation of H₂S in planetary surfaces.

Key words: astrochemistry - Earth - meteorites, meteors, meteoroids - methods: analytical - methods: laboratory: solid state

1 INTRODUCTION

Since the first detection of interstellar molecules (McKellar 1940), it has been understood that the origin of chemical complexity on Earth lies beyond the surface of our planet. With the advancement of technology, the number of molecules detected in different astrophysical environments has risen to more than 250, plus their isotopologues (Endres et al. 2016), some of them, such as H¹³CO⁺, CH₃OH, CH₃CHO or NH₂CHO having an important relation to prebiotic chemistry (see Guélin & Cernicharo (2022) for a review). Interstellar complex organic molecules (iCOMs), i.e., molecules found in space with at least 6 atoms one of them being carbon, are considered to be the precursors for the formation of more complex systems that potentially gave rise to life, which were accreted on the surface of our planet during its formation or immediately after, and evolved there. Geochemical and additional synthetic processes that occurred during the first years of planetary evolution would have used those iCOMs as reactants to promote further complex chemistry, re-combining and forming interacting and self-replicating systems (Walde 2005; Schulze-Makuch & Irwin 2008; Nakashima et al. 2018). Understanding the chemical complexity that brought life to Earth means studying where iCOMs formed, how were they delivered to Earth, and what was their role in the synthetic mechanisms towards the emergence of life that occurred during the infancy of planet Earth.

Because in most astrophysical environments conditions are harsh,

with very low gas densities and temperatures as low as 10 K, the current understanding is that most complex reactions occur in the surface of dust grains. At these very low temperatures, volatiles condense on the surface of dust grains, where molecules get closer together to form ices, and the likelihood for reactive encounters increases. Simple reactions, such as CO hydrogenation, can occur in this way and many observational and experimental works support this hypothesis (Garrod & Herbst 2006; Garrod et al. 2008; Rimola et al. 2014; Linnartz et al. 2015; Martín-Doménech et al. 2020; Enrique-Romero et al. 2022). However, these models only reflect the role of the dust grain as a third body, increasing the density of the molecules on its surface, and absorbing the excess energy of the reaction to prevent the new molecule from dissociating (Ferrero et al. 2023). In these models, reactions are mostly governed by the interactions of molecules with the ice, and generally any reactivity from the grain itself is ignored. Hence, they are only valid in regions where dust grains are covered in ices, and do not take into account situations where the grains are bare (Bennett et al. 2013; Marchione et al. 2019; Potapov et al. 2020) or consider warmer environments where ices might not present, such as very energetic regions of outflows or accretion or asteroidal and planetary surfaces.

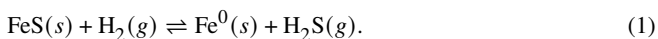
Chondritic meteorites are one of the closest samples that we can get nowadays from the dust that was present in the protoplanetary disk during the formation of the Solar System. Chondrites come from undifferentiated parent bodies, which were formed from the agglomeration of dust grains, and which experienced very low chemical or thermal alteration during their lifetime (Zolensky et al. 2008), hence preserving their pristine composition, allowing us to study the

* E-mail: v.cabedo@hw.ac.uk

evolution of the primordial protoplanetary dust. Chondrites are agglomerations of different components ranging from submillimeter- to centimeter-size and which include: chondrules, Ca-Al-rich inclusions (CAIs), aggregates of olivines and other silicates, transition metal inclusions, such as Fe and Ni, metal oxides, such as Fe₂O₃, and sulfur-bearing compounds, such as FeS (Weisberg et al. 2006). Chondrites can be of three different classes, Enstatite (EC), Ordinary (OC) or Carbonaceous (CC), which differ in their refractory abundances with respect to solar abundances. Each class is, at the same time, sub-divided in different types, such as CMs or CVs (CCs), or H, L and LL (OCs). For a complete description of the classification of chondrites and their characteristics, see Weisberg et al. (2006). Chondrites also comprise the largest proportion of meteorites falling to Earth surface, with CCs being particularly important, due to their high content in carbonaceous material.

Recent studies suggest that the minerals present in meteorites and hence in dust grains, such as silicates, or other inclusions, such as transition metals or metallic oxides, can have proper catalytic activity, i.e., can lower activation energies and/or promote new reaction mechanisms when interacting with the gas and/or the liquid phase on their surface (Llorca & Casanova 1998, 2000; Ferrante et al. 2000; Kress & Tielens 2001; Rotelli et al. 2016; Cabedo et al. 2021; Peters et al. 2023; Pareras et al. 2023, 2024). The material present in the solid phase during the star formation process would have been inherited and delivered to accreting protoplanets, and would have enhanced the chemical complexity of the forming planets, potentially promoting chemistry which is key to the origin of life (Birnstiel et al. 2016; Nakashima et al. 2018). In this context, meteoritic material can be of key importance for the delivery of solids, water, and already formed complex molecules, but also for the chemical evolution on the early Earth surface, and hence for pre-biotic chemistry.

The metallic elements present on chondrites are well known on Earth for their catalytic properties, which are widely used in the industry. For example, Fe and iron oxides catalysts are extensively used for processes such as the production of fuels through the Fischer-Tropsch (FT) process (Mahmoudi et al. 2017), or the production of NH₃ through the Haber-Bosch (HB) mechanism (Liu 2014). Previously, some of the present authors presented an experimental study showing the reactivity of chondritic material, and in particular their metallic inclusions, towards the formation of small hydrocarbons following the FT mechanism (Cabedo et al. 2021). Additionally, we have performed computational analysis that point towards the potential ability of single atom particles present in dust grains to carry out the formation of small hydrocarbons and alcohols through the FT (Pareras et al. 2023, 2024). Here, we aimed at extending both the experimental and computational work towards the direct hydrogenation of chondritic material with H₂, under a N₂ atmosphere at appropriate protoplanetary conditions. In particular, we aim at proving the hydrogenation of FeS towards the production of H₂S and metallic Fe, following:



We follow the same experimental procedure as in Cabedo et al. (2021), but we change the analysis system for a Cu(SO₄)₂ solution (see the Section 2), expecting that the formed H₂S will dissolve in water, and S²⁻ ions will quickly react with Cu²⁺ and precipitate in the form of Cu₆S₆. We complement the experimental study with a computational evaluation of the viability of the mechanism at the experimental conditions. We present here the results and discuss its implication towards chemical evolution in different astrophysical environments, in particular on the primitive Earth surface.

2 EXPERIMENTAL PROCEDURE

2.1 Sample description and preparation

Different samples were used to check the reactivity under the given conditions. Meteoritic samples are chosen to prove their surface reactivity. They are provided by different collections and used according to their availability. CCs and OCs are chosen because of their primitive composition, and their relative low degree of alteration and lack of phase differentiation. CCs are characterised by having Mg/Si ratios near solar value and O isotopic composition near or below the terrestrial fractionation line while OCs are distinguished by presenting sub-solar Mg/Si and refractory/Si ratios, to exhibit O isotope composition above the terrestrial fractionation line. These characteristics make them good representatives of the composition of the dust present in the protoplanetary disks and the surfaces of protoplanets during accretion (Weisberg et al. 2006). Both classes are also representative of the largest numbers of meteoritic falls on Earth surface and, by extrapolation, of the material that fell on Earth during the first stages of planetary evolution.

Allende is the largest CC to have fall on Earth, emitting an impressive fireball, in the early morning of 1969, in Pueblito de Allende, Mexico. Numerous specimens of this meteorite have been recovered during the years, making it one of the most studied meteorites. Allende is classified as a CV which are characterised by having an abundant matrix (up to 40 vol%), large chondrules (mm sized) many of which are surrounded by igneous rims, and a high abundance of Calcium-Aluminium-Inclusions (CAIs). Allende is an oxidised CV meaning that it has a coarser matrix and is more extensively altered than its reduced counterparts. All CVs are of petrologic type 3, which have abundant chondrules, present low degrees of aqueous alteration and have unequilibrated mineral distributions.

Murchison fell in 1969 near Murchison, Australia. Due to its large mass it is also a very well studied meteorite. It became very well known due to the large diversity of organic compounds detected on its interior (Schmitt-Kopplin et al. 2010). Classified as a CM, Murchison is one of the least-altered chondrites. CMs are distinguished by small chondrules and refractory inclusions (0.3 mm), abundant matrix (around 70 %), and abundant hydrated minerals such as phyllosilicates. Murchison is of petrologic type 2, where only some silicates have been aqueously altered. CM-like material usually occurs in clasts in other chondrite groups and achondrites, suggesting a wide distribution of the material in the early solar system (Zolensky et al. 1996; Weisberg et al. 2006). Both Allende (Sample A) and Murchison (Sample B) were obtained as fine ground powders.

KG 007 is an OC of subtype H and petrological type 6. OCs contain a large volume percentage of chondrules, with only 10-15 vol% of fine-grained matrix. They do not contain organic matter in their matrix. The H (high-iron) group of OCs are characterised by their high siderophile element content, with metal abundance of around 8 vol%. Petrological type 6 designates chondrites that have been metamorphosed under conditions sufficient to homogenise all mineral compositions, but melting did not occur. KG 007 was obtained fully ground and in two different phases: one containing the full meteoritic composition (Sample C) and another one containing only metallic inclusions separated by magnetic means (Sample D).

Silicate samples of serpentine and pyroxene, which are minerals commonly found in meteorites (Weisberg et al. 2006), are used to assess where the reactivity is originating and if it is due to the presence of silicates, the potential catalytic ability of the metallic inclusions or other type of reactivity.

Additionally, we made three different blank experiments: one only with the stainless steel (SS) reactor (Sample G), one with only SiC

(Sample H) and one containing a sample of KG 007 (full composition) and 40 ml/min of N₂ (Sample I) to prove that products are not produced by the out-gassing of the meteorite. Finally, the FeS experiments (Sample J-J.5) are carried out with commercial FeS from Thermo Fischer Scientific ©, with 99.9 % purity, and a mesh size of 100 μm.

Preparation of the samples prior to introduction on the reactor is explained in our previous work (Cabedo et al. 2021).

2.2 Experimental set-up for measuring the samples reactivity

The total weight of the samples is introduced in a stainless steel (SS) reactor heated by a furnace where a flux of H₂ and N₂ are circulated. Gaseous products are circulated through a quartz bubbler and collected in a 0.1 M Cu(SO₄)₂ solution. We expect the production of H₂S following Eq. 1, and the subsequent precipitation of Cu₆S₆. Cu is chosen for its ability to react, the high constant of the reaction for the solid precipitation, and the easiness of qualitatively identifying the production of Cu₆S₆ as a black solid. Additionally, it allows its quantification by collecting the resulting Cu₆S₆. Any solid left on the bubbler is scraped and left in the solution, which is transferred to a conic bottom flask and left to deposit the solid. The liquid is then decanted, and the solid is rinsed with water and decanted again, three times. The solid is extracted from the flask with acetone, and left to dry for 48 h at 80 °C. Finally, the solid is weighed. The error in this procedure can be high and unknown, due to the difficulty of removing all the solid precipitated inside of the bubbler, however, it makes a qualitative assessment extremely simple and provides a lower-limit for the reaction considered.

Reaction conditions are chosen to resemble those present in different warm astrophysical environments, such as dust grains in solar nebulae experiencing high temperature conditions (shocks, accretion streams), or the surface of rocky protoplanets, like Earth.

- The ratio of reactants was set to H₂:N₂ = 3, as a likely ratio present in the solar nebula or a primitive Earth atmosphere (Zahnle et al. 2010; Wordsworth 2016). The fluxes of the reactants were set to a total of 40 mL/min, with H₂ ≈ 32 mL/min and N₂ ≈ 8 ± 1 mL/min.

- The temperature is set at 873 K. This is a relevant temperature for the type of reactions studied, which can be achieved in the astrophysical environments proposed.

- Reactions are left to proceed for 48 h, in order to accumulate as much solid product as practically possible.

2.3 Characterisation of solid products by X-Ray diffraction

To analyse the samples through X-Ray Diffraction (XRD), a small amount (few mg) of the dried solid produced during the reaction is taken to an X-Ray diffractometer in order to assess its composition and crystallographic structure. The powder is dispersed in isopropyl alcohol on a silicon zero background holder. Data were collected on a Malvern Panalytical MultiCore Empyrean diffractometer with generator settings of 40 mA and 45 kV. The sample holder was placed on the Reflection-Transmission Spinner stage and the sample was rotated at 15 rpm. Intensity data were collected in Goni mode (Bragg-Bretano geometry). Data were collected in the range of 5-85 in 2θ. The Step size was 0.0260 ° and the scan time was around 30 mins. The diffraction pattern was analysed using the HighScore software package from Malvern Panalytical. Automated background subtraction, peak identification and searching of the Powder Crystallographic open database was performed with pre-programmed batch “IdeALL” provided in HighScore. Fit of likely patterns was checked

with basic Rietveld refinement using the MultiRiet script and the Chi Square, R_p, R_{wp} and R_{exp} values.

2.4 Magnetic susceptibility analysis

The magnetic susceptibility, χ , is the ability of a magnetic material to react to an external magnetic field. Following:

$$M = \chi H \quad (2)$$

it relates a material’s magnetisation, M , with the strength of an applied magnetic field, H . Conventionally, these terms are assumed to be linearly dependent, which is true for high temperatures and low fields. Typically, magnetic susceptibility has been measured by determining the apparent weight of a sample under a magnetic field, but more precise and simpler techniques have been developed in the recent years that allow for a quick characterisation of the magnetic properties of samples. For a complete description on magnetic susceptibility see Mugiraneza & Hallas (2022). In here, it suffices to say that we are interested in detecting any change in the susceptibility of the samples before and after the reaction, which would implicate a change in the magnetic composition, and potentially, the metallic one. Since our samples are very heterogeneous, we define a total specific susceptibility, χ_s , for the complete sample by measuring the given susceptibility, χ , and dividing by the total mass of each sample, m :

$$\chi_s = \chi/m \quad (3)$$

Measurements of the magnetic susceptibility of the samples are done with a magnetic susceptibility meter from ZH Instruments. The measurements are done by introducing a representative amount of each sample in a plastic bag and shaped in a layer of around 5mm of thickness. Measurements are taken directly next to the samples with no air gap between the instrument and the samples, so no thickness correction needs to be applied. We measure the magnetic susceptibility before the reaction, χ_s^0 , by taking a representative amount of the samples without reacting (i.e. the meteoritic material), and the magnetic susceptibility after reaction, χ_s^r , by taking the whole amount of the diluted samples once reacted.

2.5 Computational details

The reactive surfaces were modelled using a periodic approach. Quantum chemical calculations were performed with the CP2K package (Kühne et al. 2020). The characterization of the potential energy surface (PES) of the reactions requires determining the structures and the energetics of the stationary points. For geometry optimizations, the semi-local PBE_{sol} functional was used (Perdew et al. 2008), along with the Grimme D3(BJ) correction to include dispersion forces (Grimme et al. 2010). A double- ζ basis set (DZVP-MOLOPT-SR-GTH gaussian basis set) was adopted for all the atom types, combined with a cut-off set at 500 Ry for the plane wave auxiliary basis set (VandeVondele et al. 2005; Kühne et al. 2020). The Goedecker–Teter–Hutter pseudopotentials were used to describe core electrons, while a mixed Gaussian and plane-wave (GPW) approach was employed for valence electrons (Goedecker et al. 1996).

The bulk of troilite (stoichiometric FeS) exhibits an hexagonal structure (space group P6̄2c), with XRD crystallographic cell parameters of $a = b = 5.896$ (Å) and $c = 11.421$ (Å), and $\alpha = \beta = 90$ degrees and $\gamma = 120$ degrees, which upon PBE_{sol} optimization

convert into $a = 5.697$ $b = 5.580$ (Å) and $c = 10.208$ (Å), and $\alpha = \beta = 90$ degrees and $\gamma = 120$ degrees. A recent study considering different slabs generated automatically by the code POLYCLEAVER (Mates-Torres & Rimola 2024), concluded that the most stable surface is 011 (Martinez-Bach et al. 2024), and so we choose that surface for all our studies. To approach our system to reality we generated different defects by means of Fe vacancies. The FeS(011) structure shows a combination of tetra- and penta-coordinated Fe atoms, to generate the defective structures rationally, we have constructed geometries in which the vacancies are from a tetra-coordinated Fe (Tetra-Def) or a penta-coordinated (Penta-Def). Moreover, we have also considered the combination of multiple defects on the same structure, removing in this case two tetra- or penta-coordinated irons (Tetra-Def-2 and Penta-Def-2 respectively) or one of each Fe (Tetra-Penta-Def). Note that to maintain the stoichiometry (and hence the electroneutrality), the relevant S atoms were removed from the opposite face of the slab.

The climbing image nudged elastic band (CI-NEB) technique implemented in CP2K (Kühne et al. 2020) was used to search for transition states. The CI-NEB calculations were also run at PBEsol-D3(BJ) level. Activation energy barriers were calculated as

$$\Delta E^{\ddagger} = E_{TS} - E_{GS}, \quad (4)$$

$$\Delta U^{\ddagger} = \Delta E^{\ddagger} + \Delta ZPE, \quad (5)$$

$$\Delta G_T^{\ddagger} = \Delta E^{\ddagger} + \Delta G_T, \quad (6)$$

where ΔE^{\ddagger} is the potential energy barrier, in which E_{TS} and E_{GS} are the absolute potential energies for the transition state and the local minimum structure, respectively, ΔU^{\ddagger} is the vibrational zero-point energy (ZPE) corrected barrier, in which ΔZPE refers to the contribution of the ZPE corrections to ΔE^{\ddagger} , and ΔG_T^{\ddagger} the Gibbs activation barrier at a given temperature, in which ΔG_T refers to the contribution of the Gibbs corrections to ΔE^{\ddagger} . Note that final Gibbs energies have been computed at the working temperature of 800 K.

The nature of the stationary points of the reactions was validated by calculating the harmonic frequencies; the outcome being minima for reactants, intermediates and products, and first-order saddle points for transitions states. Vibrational harmonic frequencies were calculated at the PBE_{sol}-D3BJ/DZVP-optimized structures using the finite differences method as implemented in the CP2K code (Kühne et al. 2020). To minimize the computational cost, a partial Hessian approach was employed. Consequently, vibrational frequencies were computed for a subset of the entire system, comprising only the surface atoms participating in the reaction and the reactive species.

3 RESULTS

3.1 Reactivity of the chondritic meteorites towards the formation of H₂S

In this section we describe the results regarding the reactivity of the chondritic meteorites under reducing conditions. The different samples, and the results for all the experiments are summarised in Table 1. First, we carried out the blank experiments (samples G, H and I). No precipitate is formed so we can confirm that i) there is no activity coming from the SS reactor or from the SiC used as solvent, and ii) no product formed is the result of out-gassing of the samples.

For all meteoritic samples (A, B, C and D), a black solid is observed precipitating in the solution soon after reaction starts. The

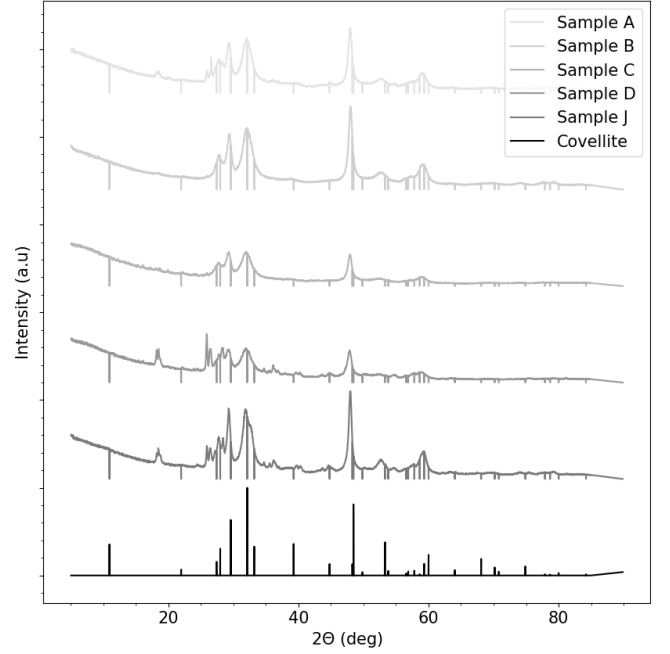


Figure 1. X-Ray Diffraction patterns of Covellite (bottom) and the recovered products. The downward lines in the spectra correspond to the theoretical position of the covellite peaks. Note that Samples E and F are not shown due to a lack of sample to perform the XRD analysis.

same black precipitate is observed when reacting the silicate samples (Samples E and F). In the case of pyroxene (Sample E) the amount of solid formed was so small that it was not possible to retrieve it from the solution. XRD patterns of the recovered solid are shown in Fig. 1, which shows that the solid obtained is Cu₆S₆ (Covellite) in all cases. The experimental spectrum of covellite is shown for comparison (Takéuchi et al. 1985; Downs & Hall-Wallace 2003). The downward lines in the experimental spectra correspond to the theoretical position of the covellite peaks. Additional peaks correspond to Poitevinite, a phase of Cu(SO₄)₂ left as a residue from the used solution. In order to confirm that the produced Cu₆S₆ is due to the reduction of FeS, we perform the same experiment with commercial FeS as reactant (Sample J). The production of Cu₆S₆ in the solution was also observed, confirmed by the XRD pattern (Fig. 1), which allows us to confirm that a mechanism similar to Eq. 1 is happening.

The reaction of the sulfides present in the samples with H₂ should increase the magnetic properties of the sample for two reasons: i) the removal of Fe and S atoms from the troilite (FeS) lattice and the subsequent formation of pyrrothites (Fe_{1-x}S) of unknown stoichiometry increases the magnetisation of the samples since the former is non-magnetic but the later is (Dorogina et al. 2015), and ii) the formation of metallic Fe and iron oxide nanoparticles with strong magnetic properties (Woo et al. 2004). Hence, we measured the magnetic susceptibility before (χ_s^0) and after (χ_s^r) reaction. The results of these measurements is shown in Table 1. There is a clear increase in the χ_s values before and after reaction, suggesting an increase on the magnetic components of the sample, and further confirming that the mechanism proposed is taking place. The change in the magnetism of FeS is evident in Sample J where the only phase present initially is troilite. However, the obtained values suggest that additional re-

[!ht]

Table 1. Sample description and results

	Sample	Weight (g)	Cu ₆ S ₆ weight (g)	FeS (%wt)	FeS (%vol)	χ_s^0 (g ⁻¹)	χ_s^r (g ⁻¹)	$\Delta\chi_s$ (g ⁻¹)
A	Allende	0.5002	0.0211	17.3	10.48	0.1331	1.353	1.220
B	Murchison	0.5000	0.0200	16.4	8.52	0.2249	3.250	3.025
C	KG007	0.5000	0.0045	3.5	2.69	0.7616	3.710	2.948
D	KG007 (magnetic phase)	0.5001	0.0057	4.7	-	1.333	4.539	3.205
E	Pyroxene	0.5003	< 0.0001	< 0.1	-	0.1706	0.6646	0.4939
F	Serpentine	0.5002	0.0007	0.6	-	0.0375	0.4368	0.3992
G	SS* blank	-	-	-	-	-	-	-
H	SiC blank	0	0	-	-	-	-	-
I	KG007 blank	0.5004	0	-	-	0.7616	2.188	1.426
J	FeS	0.5002	0.0423	-	-	0.0148	1.9462	1.931

Instrumental errors are ± 0.0001 g. Errors for the percentages on weight and volume are derived from instrumental errors and are of the order of ± 0.1 .

* Stainless steel (SS)

actions are taking place which cannot be quantified. We discuss this further in Section 3.2.

We can estimate the amount of FeS in our samples by deriving the reaction rate, k , for Eq. 1 from the commercial sample by making certain assumptions. First we assume that the composition of the commercial FeS sample is uniform, and that only 69.2 % is FeS, all in the form of troilite, which reacts with H₂. Secondly, we assume that H₂ has a large enough contact time with the sample to react completely, and that the contact is isotropic and equal through all the reactor. Finally, we assume that the reaction rate is constant through all the reaction time, as there is enough of both reactants. We can derive k such as:

$$k = \frac{n_{H_2S}^f}{g_{FeS}t} \quad (7)$$

where $n_{H_2S}^f$ are the number of mols of H₂S that have been produced, g_{FeS} is the initial mass of FeS in the commercial sample, in grams, and t is the reaction time (which in the case of Sample J is 24 h). We obtain a value of $8.877 \pm 0.002 \times 10^{-7}$ mol min⁻¹ g⁻¹ at 873 K. With this value in hand, and assuming that all the different phases of FeS present in the samples react with the same rate constant as troilite, and that the grain size is similar through all the samples and its influence on the reaction rate is negligible, we can approximate the percentage in weight (%wt) of FeS in the totality of the samples. To obtain the percentage in volume (%vol) we use bulk density values for Samples A, B and C of 2.8, 2.4 and 3.7 g cm⁻³ respectively (Flynn et al. 1999), and a density value of 4.6 g cm⁻³ for Sample J (Armbruster & Danisi 2016).

In the literature, the sulfide content in chondrites varies depending on the type and alteration history of the parent body to which the sample belongs to. For CMs, which have suffered a certain degree of aqueous alteration (Brearley 2006; Singerling & Brearley 2018), the %vol ranges from 0.6 to 5.9, with 1.8 %vol for Murchison (Howard et al. 2010, 2015; Schrader et al. 2021). We obtain a larger value of 8.52 % vol. Less altered CVs show larger ranges and higher values, from 1.9 to 9.9 %vol, with 6.6 %vol for Allende (Howard et al. 2010; Schrader et al. 2021). OCs of type H show various degrees of alterations, H6 are highly thermally and aqueously altered and show more restricted values and higher, from 4.1 to 7.0 (Schrader et al.

2021; Dunn et al. 2010). Our values seem to be slightly too high for CCs but slightly too low for the OCs. We note that the scope of this work was not to accurately determine the amount of sulfides in chondritic meteorites, but to prove their reactivity, and so we consider that our results are close enough to values in the literature to consider our hypothesis valid. However, we note here some reasons why our values might be slightly inaccurate. First, we note that in the literature the most common technique to determine the composition of a sample is XRD, although other techniques, such as Electron Microscopy (EM) can be used. XRD is considered accurate up to ± 2 %, as long as the sample that is being analysed is considered representative of the whole sample, and the fitting of the spectral matching is good (Bland et al. 2004). On the other hand, our method contains many approximations, which have been mentioned through the text, and is a simplification of what is possibly a complicated network of chemical reactions and changes in the solid phase. Particularly important are the assumptions on the reaction rates and the densities used to obtain the %vol. Additionally, our ability to replicate the experiments in order to obtain independent measures is completely restricted by the amount of samples that we can analyse. Finally, we note that we cannot recover all the Cu₆S₆ from the solution, and so we can only present a minimum of the FeS measured through this method.

Nevertheless, we can make a rough analysis of the relation between the alteration degree, and the amounts of FeS found in our sample. Sulfur containing minerals are believed to condense from the solar nebula mostly in the stoichiometric form of troilite, and is later processed through aqueous and thermal alteration, becoming an indicator of the alteration degree of the parent object (Zolensky & Thomas 1995; Kimura et al. 2011; Schrader & Zega 2019; Schrader et al. 2021). We find that the amount of product, and hence the amount of FeS found in the sample correlates well with the degree of alteration, as we find a decreasing amount of FeS (OC \leq CM \leq CV) with increasing alteration degree (OC \geq CM \geq CV). Additionally, this points to the fact that the phase more susceptible to hydrogenation is troilite. Sulfurisation processes, i.e., the formation of troilite phases from H₂S and Fe (Lauretta et al. 1998), could be occurring once H₂S is formed in the reactor, however, we have no evidence of that and instead our results point towards the reverse process being more favourable at the reaction conditions.

Finally, we can estimate the activation energy of the reaction,

E_a , by performing additional experiments with commercial FeS at temperatures from 323 to 873 K. We observe that at 573 K some Cu_6S_6 is produced, however, the amount is minimum and cannot be recovered. Below that temperature, no Cu_6S_6 production is observed and no results are presented. Details of these experiments are shown in Table 2.

We derive the activation energy of the reaction from the Arrhenius equation:

$$k = A \exp \frac{-E_a}{k_B T} \quad (8)$$

where A is the pre-exponential factor (in $\text{mol min}^{-1} \text{g}^{-1}$), k_B is the Boltzmann constant (in $\text{kcal mol}^{-1} \text{K}^{-1}$) and E_a is the activation energy (in kcal mol^{-1}). We find that the reaction constant behaves linearly between 573 and 723 K, and then flattens. Following Eq. 8, we find $E_a = 44.4 \text{ kcal mol}^{-1}$. We discuss this value along with the computational results in Section 3.4.

3.2 Further reactivity of the samples

When looking at the magnetic susceptibility results, we observe interesting features that point to additional reactivity not related to the production of H_2S . First, the increase in the magnetic susceptibility of Sample I is striking. Since H_2 is not present in this experiment we attribute the increase to the thermal decomposition and phase changes of different compounds in the sample, such as FeS (pyrrhotites, but also troilite) (Suttle et al. 2021) and Fe oxides (Jozwiak et al. 2007). Additionally, N_2 could participate in reactions with Fe compounds that we cannot detect, but this scenario is unlikely. Although NS, and related molecules, are widely observed in different regions of space (McGonagle et al. 1994; McGonagle & Irvine 1997; Sanz-Novo et al. 2024) their formation in the experimental conditions is complicated due to the low reducing capacity of N_2 and an unfavourable mechanism (Pereira et al. 2010). Abundance of nitrogen oxides, such as NO, is also large in the ISM (Dupuy et al. 2017), but the direct reduction of Fe oxides with N_2 seems unlikely. We note as well, that no production of NH_3 is observed through the HB mechanism, which would be seen by the precipitation of $\text{Cu}(\text{OH})_2$, a light blue solid, in the solution.

Secondly, we note that the increase in magnetic susceptibility is not directly correlated with the amount of FeS found for each sample, additionally suggesting that other reactions are taking place. In addition to all the possible reactions already mentioned, iron oxides, largely present in all of the samples, can be reduced in the presence of H_2 to form other oxides, metallic iron, and water, at the reaction temperature (Jozwiak et al. 2007), contributing to the increase of magnetic susceptibility by producing metallic Fe. Reduction of iron silicates can also be occurring (Massieon et al. 1993) to give metallic Fe. This process can be hinted at with Samples E and F which contain very low amounts of FeS and have a very low initial magnetic susceptibility, which increases substantially after the reaction has taken place.

Finally, we need to consider that our samples contain different phases of sulfides: the most abundant are of the pyrrhotite group (Fe_{1-x}S where $0 \leq x \leq 0.125$, but can be up to 0.2). In addition, it can also occur in forms of pyrite (FeS_2) and pentlandine ($(\text{Ni,Fe})_x\text{S}_{x-1}$) inclusions (Bullock et al. 2005; Singlering & Brearley 2018; Schrader et al. 2021). In this work we are only considering the reduction of pure troilite, but reduction of other phases would also result in the formation of H_2S and metallic Fe, as well as an increase on the magnetic susceptibility.

While we acknowledge that we cannot directly correlate the change in magnetic susceptibility to a particular reaction, we consider that it is evidence enough of the general reduction of the material. Since we cannot measure any of the additional products of the reduction with the simple experimental procedure, and the different samples contain different amounts and forms of iron oxides and silicates, we cannot derive any reaction constants or provide any further characterisation. Further experiments with a more detailed separation and characterisation of the reaction products are needed.

3.3 Computational characterisation of the reaction mechanism

To complement our study, we provide density functional theory (DFT) calculations to characterise the mechanisms and derive the energetics of the H_2S formation following Eq. 1. Although the nature of the FeS in the meteoric samples is diverse, we select a pure troilite structure to perform the calculations, following the procedure described in Section 2.5.

The reaction mechanism that we propose based on Eq. 1 proceeds through four steps (see Fig. 3): first, the adsorption of H_2 , second and third, the successive H transfers from the Fe to the S, and finally the desorption of H_2S . We have constructed the PES for each of the proposed defective surfaces. In this section, we comment the obtained energies and the viability of the mechanism. A complete summary of the values can be found in the Supplementary Information.

The H_2 adsorption can only happen on two possible positions: on the penta-coordinated or on the tetra-coordinated Fe surface atoms. The later showing larger stabilisation energies upon H_2 adsorption, because H_2 breaks in a homolytic fashion. Once H_2 has been adsorbed, the mechanism proposed proceeds through two hydrogen transfers from the Fe to the S, each of them with an associated energetic barrier. The values for the barriers and the reactions of the different proposed systems are shown in Table 3. If we consider the systems where H_2 has been absorbed onto a penta-coordinated Fe, for the first hydrogenation we see values between 16 kcal mol^{-1} and 23 kcal mol^{-1} , and, in most of the cases, this step is endergonic. The second hydrogenation has slightly higher energy barriers. In all cases we see a reduction in the barrier when increasing the number of defects. The reported Gibbs energies show that the final hydrogenation is endergonic. For systems where H_2 is absorbed in the tetra-coordinated Fe, the H_2 adsorption is slightly more favourable. The first hydrogenation also proceeds with slightly lower energy barriers, reaching its lowest at 1 kcal mol^{-1} . This process is also exergonic for the more reactive configurations. Finally, barriers for the second hydrogen transfer show to be substantially higher, due to the over stabilisation of the remaining H on the surface. Calculated values for the Gibbs energies for the last step also show that all the processes are endergonic. In summary, differences are observed between the different systems, however, although we treat the results as individuals one needs to consider that the real picture of the process will be a combination of all of them.

3.4 H_2S desorption

Finally, we study the desorption of H_2S from the surface. Despite the differences amongst the different systems, desorption energies are always above 40 kcal mol^{-1} . The different energetic values between the systems can be attributed to the different geometrical reorganisation after H_2S desorption. In all cases, breaking the H_2S -Fe bond is highly energy demanding, and the final surface becomes highly unstable. This value is in agreement with the experimental value found

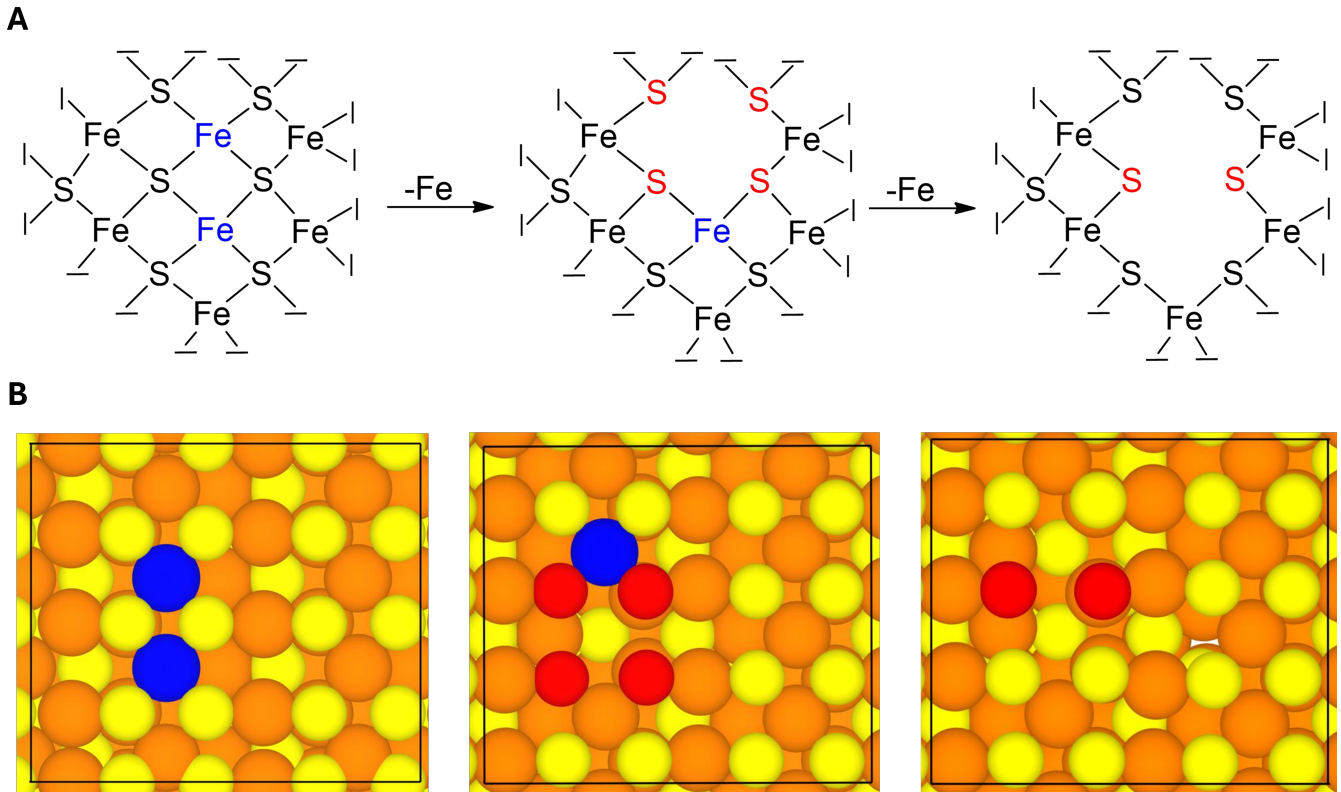


Figure 2. Panel A: Schematic representation for the formation of the Fe vacancies on the (011)FeS surface. Panel B: optimized geometries for the original, non-defective, slab, the slab with a single Fe vacancy and the slab with two Fe vacancies (S atoms are in yellow and Fe atoms in orange). Fe atoms highlighted in blue colour are the ones removed on the process. S atoms highlighted in red are the most reactive ones in each structure.

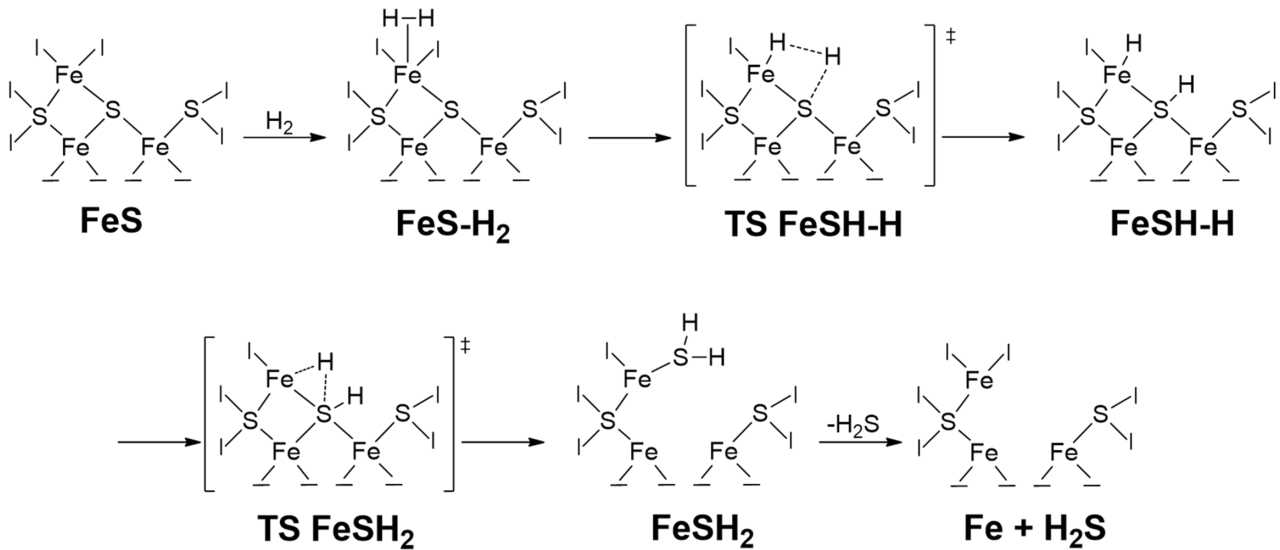


Figure 3. Proposed reaction mechanism for the H_2S formation

Table 2. Results of the FeS experiments

Sample	Temperature (K)	FeS weight (g)	Cu ₆ S ₆ weight (g)	k ($\times 10^{-7}$ mol min ⁻¹ g ⁻¹)
J	873	0.5002	0.0423	8.877
J.1	823	0.5003	0.0349	7.322
J.2	773	0.5002	0.0260	5.456
J.3	723	0.5004	0.0256	5.37
J.3	673	0.5001	0.0068	1.477
J.4	623	0.4999	0.006	1.26
J.5	573	0.5000	< 0.0001	< 1

Instrumental errors are ± 0.0001 g. Errors in the reaction rate are derived from instrumental errors and are of the order of $\pm 0.02 \times 10^{-7}$ mol min⁻¹ g⁻¹.

Table 3. Collected Gibbs-corrected energy barriers at 800K (ΔG^\ddagger) and reaction energies (ΔG^{rx}) for the different H transfers to finally form H₂S. Units are in kcal mol⁻¹.

	System	H ₂ -Penta-Fe		H ₂ -Tetra-Fe	
		TS FeSH-H	TS FeSH ₂	TS FeSH-H	TS FeSH ₂
ΔG^\ddagger	Tetra-Def	22.7	33.3	21.7	55.0
	Penta-Def	24.0	21.2	21.9	27.3
	Tetra-Def-2	18.1	26.5	17.2	48.0
	Penta-Def-2	18.6	20.1	0.1	37.5
	Tetra-Penta-Def	16.1	20.7	7.6	36.5
ΔG^{rx}	Tetra-Def	10.7	29.5	11.7	45.0
	Penta-Def	-3.7	20.1	2.59	29.4
	Tetra-Def-2	12.5	22.5	11.4	38.5
	Penta-Def-2	5.1	10.6	-12.0	24.8
	Tetra-Penta-Def	-1.1	13.8	-1.3	21.8

in this work, and points to the fact that the experimental E_a estimate reflects the desorption energy, and not the reaction energy barriers. Hence, the desorption can be understood as the rate determinant step of the mechanism.

We can compare our desorption energy result to binding energies of H₂S, which have been studied in a different set of surfaces, both experimentally and theoretically. Temperature Programmed Desorption (TPD) experiments of H₂S in water ice show a binding energy of ≈ 5 kcal mol⁻¹ (Collings et al. 2004; Jiménez-Escobar & Muñoz Caro 2011; Cazaux et al. 2022; Furuya et al. 2022). While comparison with theoretical values is difficult, due to the pre-exponential factors used to derive them (Ferrero et al. 2022; Minissale et al. 2022), experimental values agree with binding energies calculated through quantum mechanical computations, which range from 1.5 to 8.5 kcal mol⁻¹ (Oba et al. 2018; Perrero et al. 2022; Ferrero et al. 2022; Perrero et al. 2024; Bariosco et al. 2024). As it has been discussed in the literature, these low values explain why H₂S is not found in icy grain mantles, and discards H₂S as a S reservoir on ices. Binding energies of H₂S in silicates have also been studied (Perrero et al. 2024). Their work found that adsorption of H₂S in silicates is more favourable due to the dative covalent interactions between S and Mg or Fe, compared to the H-bond interactions present on ices. These covalent interactions are more stable for the S-Fe (23 kcal mol⁻¹), while the S-Mg is less stable (17-20 kcal mol⁻¹) and promotes dissociative adsorption. Their results argue that already formed H₂S present in the ISM is likely to stick to grain surfaces and become part of their cores as refractory material.

The desorption energy measured in this work is much larger (≥ 40

kcal mol⁻¹) due to the large destabilisation of the FeS surface upon H₂S desorption, compared to the silicate surfaces. Our results support the hypothesis that once in the refractory phase of dust grains, S is hard to remove at interstellar conditions, needing of very energetic events to bring it back to the gas phase. This opens the door to explain both the depletion of S from the gas phase during the first stages of star formation and the lack of detection in the icy dust grains mantles during these stages, as an important amount of S might be locked in the refractory phase of dust grains.

4 CONCLUSIONS

In view of the results, we conclude that the formation of H₂S on the FeS surface through subsequent hydrogenations is feasible at high temperatures. While the most energetic step is the desorption of H₂S from the surface (≥ 40 kcal mol⁻¹), at the working temperatures H₂S is easily released to the gas phase. We can prove that at the experimental conditions, the process is favourable and possible, however, its importance in different environments of the ISM needs to be further discussed.

Hydrogen sulphide has been identified through the years in different astronomical sources, such as molecular clouds (Thaddeus et al. 1972), star forming regions (Holdship et al. 2016), in cold regions of protoplanetary disks (Phuong, N. T. et al. 2018), and the atmospheres of some Solar System planets (Irwin et al. 2018; Irwin et al. 2019). Since the temperature in these regions is really low, between 10-150 K, this reaction would not likely produce significant quantities of

H₂S, nor allow from its desorption, and the S would remain in the solid phase, in the form of refractory FeS. At these conditions, formation of H₂S might proceed instead through direct hydrogenation of S atoms that might have been sputtered in the surface of dust grains.

While at interstellar conditions, S would remain in the refractory phase, we can envision a likely environment for the formation and release of H₂S in the surface of recently formed planets. The first Earth atmosphere was probably formed by the out-gassing of material similar to chondritic material at elevated temperatures (> 700 K), and mainly composed of CO, CO₂, H₂, N₂ and H₂O. Models show that this material might also out-gas H₂S at temperatures larger than 500 K after accreting onto the planet (Schaefer & Fegley 2010). Our results show that at the working temperatures there is no out-gassing of H₂S from the solid, suggesting that this process starts at a larger temperatures. In protoplanetary conditions, the proposed mechanism might add important quantities of H₂S in early atmospheres at relatively low temperatures, compared to H₂S out-gassing. The formed H₂S could in this conditions proceed to form other complex molecules, such as thiols (Llorca & Casanova 2000). Interestingly, H₂S is proposed to be intimately linked with the origin of life for its versatility in forming other compounds and as a possible source of energy, which remains present in living systems up to these days (Olson & Straub 2016).

In summary, our results support previous results which suggest that S is depleted from the gas phase and onto the refractory phase of dust grains. Moreover, they point towards an interesting route towards the formation of H₂S and the simple removal of S from the refractory phase to a more reactive species, capable of produce further chemistry. While the proposed reaction is only favoured in high temperature environments, it leads to important products, i.e., H₂S, which can be involved in further reactions with components present on the surface of dust grains or in the primeval Earth environment.

ACKNOWLEDGEMENTS

The Heriot-Watt University group acknowledges funding from the UK Research and Innovation and the Engineering and Physical Sciences Research Council (UKRI-EPSC) for the project *Astro-catalysis: In Operando Studies Of Catalysis And Photocatalysis of Space-abundant Transition Metals*, grant number EP-W023024-1. The group also acknowledges the services of the Mechanical Engineering Workshop of the school of Engineering and Physical Sciences (EPS), and the use of the High Performance Computer (HPC) at the Computational Engineering Research (CER) group at the Institute of Mechanical, Process and Energy Engineering (IMPEE).

The Universitat Autònoma de Barcelona group acknowledges funding within the European Union's Horizon 2020 research and innovation program from the European Research Council (ERC) for the project *Quantum Chemistry on Interstellar Grains* (QUANTUM-GRAIN), grant agreement No 865657, and the funding within the Marie Skłodowska-Curie Actions (MSCA) Postdoctoral Fellowships program from the European Commission for the project *Computational Studies on Heterogeneous Astro-catalysis of Space-Abundant Transition Metals* (CHAOS), grant agreement HEU-101105235-CHAOS. G.P. thankfully acknowledges financial support by the Spanish Ministry of Universities and the European Union's Next Generation EU fund for a Margarita Salas contract. Spanish MICINN is also acknowledged for funding the projects PID2021-126427NB-I00 and CNS2023-144902. The authors thankfully acknowledge RES resources provided by Univ. Valencia for the use of Tirant (activity QHS-2022-2-0022) and by BSC for the use of MareNostrum (activ-

ity QHS-2023-1-0019). The supercomputational facilities provided by CSUC are also acknowledged. The EuroHPC Joint Undertaking through the Regular Access call project no. 2023R01-112, hosted by the Ministry of Education, Youth and Sports of the Czech Republic through the e-INFRA CZ (ID: 90254) is also acknowledged.

J.L. is a Serra Hünter Fellow and is grateful to the Institució Catalana de Recerca i Estudis Avançats (ICREA) Academia program and project GC 2021 SGR 01061.

DATA AVAILABILITY

Supporting material for the computational analysis, including Cartesian coordinates of the optimised minima and TS, the vibrational analysis and examples of input and output files can be found in the associated Zenodo repository (<https://doi.org/10.5281/zenodo.13322595>).

REFERENCES

- Armbruster T., Danisi R. M., eds, 2016, *Highlights in Mineralogical Crystallography*. De Gruyter (O), Berlin, München, Boston, doi:doi:10.1515/9783110417104, <https://doi.org/10.1515/9783110417104>
- Bariosco V., Pantaleone S., Ceccarelli C., Rimola A., Balucani N., Corno M., Ugliengo P., 2024, *MNRAS*, **531**, 1371
- Bennett C. J., Pirim C., Orlando T. M., 2013, *Chemical Reviews*, **113**, 9086
- Birnstiel T., Fang M., Johansen A., 2016, *Space Science Reviews*, **205**, 41–75
- Bland P. A., Cressey G., Menzies O. N., 2004, *Meteorit. Planet Sci.*, **39**, 3
- Brearley A. J., 2006, in Lauretta D. S., McSween H. Y., eds., *Meteorites and the Early Solar System II*. p. 584
- Bullock E. S., Gounelle M., Lauretta D. S., Grady M. M., Russell S. S., 2005, *Geochim. Cosmochim. Acta*, **69**, 2687
- Cabedo V., Llorca J., Trigo-Rodríguez J. M., Rimola A., 2021, *A&A*, **650**, A160
- Cazaux S., Carrascosa H., Muñoz Caro G. M., Caselli P., Fuente A., Navarro-Almáida D., Rivière-Marichalar P., 2022, *A&A*, **657**, A100
- Collings M. P., Anderson M. A., Chen R., Dever J. W., Viti S., Williams D. A., McCoustra M. R. S., 2004, *MNRAS*, **354**, 1133
- Dorogina G. A., Gulyaeva R. I., Selivanov E. N., Balakirev V. F., 2015, *Russ. J. Inorg. Chem.*, **60**, 301
- Downs R., Hall-Wallace M., 2003, *American Mineralogist*, **88**, 247
- Dunn T. L., Cressey G., McSween Harry Y. Jr. J., McCoy T. J., 2010, *Meteorit. Planet Sci.*, **45**, 123
- Dupuy R., et al., 2017, *A&A*, **606**, L9
- Endres C. P., Schlemmer S., Schilke P., Stutzki J., Müller H. S., 2016, *Journal of Molecular Spectroscopy*, **327**, 95
- Enrique-Romero J., Rimola A., Ceccarelli C., Ugliengo P., Balucani N., Skouteris D., 2022, *The Astrophysical Journal Supplement Series*, **259**, 39
- Ferrante R. F., Moore M. H., Nuth J. A., Smith T., 2000, *Icarus*, **145**, 297
- Ferrero S., et al., 2022, *MNRAS*, **516**, 2586
- Ferrero S., Pantaleone S., Ceccarelli C., Ugliengo P., Sodupe M., Rimola A., 2023, *The Astrophysical Journal*, **944**, 142
- Flynn G. J., Moore L. B., Klöck W., 1999, *Icarus*, **142**, 97
- Furuya K., Oba Y., Shimonishi T., 2022, *ApJ*, **926**, 171
- Garrod R. T., Herbst E., 2006, *A&A*, **457**, 927
- Garrod R. T., Widicus Weaver S. L., Herbst E., 2008, *ApJ*, **682**, 283
- Goedecker S., Teter M., Hutter J., 1996, *Phys. Rev. B*, **54**, 1703
- Grimme S., Antony J., Ehrlich S., Krieg H., 2010, *The Journal of Chemical Physics*, **132**, 154104
- Guélin M., Cernicharo J., 2022, *Frontiers in Astronomy and Space Sciences*, **9**, 787567
- Holdship J., et al., 2016, *Monthly Notices of the Royal Astronomical Society*, **463**, 802

- Howard K. T., Benedix G. K., Bland P. A., Cressey G., 2010, *Geochim. Cosmochim. Acta*, **74**, 5084
- Howard K. T., Alexander C. M. O. D., Schrader D. L., Dyl K. A., 2015, *Geochim. Cosmochim. Acta*, **149**, 206
- Irwin P. G. J., Toledo D., Garland R., Teanby N. A., Fletcher L. N., Orton G. A., Bézard B., 2018, *Nature Astronomy*, **2**, 420
- Irwin P. G., Toledo D., Garland R., Teanby N. A., Fletcher L. N., Orton G. S., Bézard B., 2019, *Icarus*, **321**, 550
- Jiménez-Escobar A., Muñoz Caro G. M., 2011, *A&A*, **536**, A91
- Jozwiak W., Kaczmarek E., Maniecki T., Ignaczak W., Maniukiewicz W., 2007, *Applied Catalysis A: General*, **326**, 17
- Kimura M., Grossman J. N., Weisberg M. K., 2011, *Meteorit. Planet. Sci.*, **46**, 431
- Kress M. E., Tielens A. G. G. M., 2001, *Meteorit. Planet. Sci.*, **36**, 75
- Kühne T. D., et al., 2020, *The Journal of Chemical Physics*, **152**, 194103
- Lauretta D. S., Lodders K., Fegley B. J., 1998, *Meteorit. Planet. Sci.*, **33**, 821
- Linnartz H., Ioppolo S., Fedoseev G., 2015, arXiv e-prints, p. arXiv:1507.02729
- Liu H., 2014, *Chinese Journal of Catalysis*, **35**, 1619
- Llorca J., Casanova I., 1998, *Meteorit. Planet. Sci.*, **33**, 243
- Llorca J., Casanova I., 2000, *Meteorit. Planet. Sci.*, **35**, 841
- Mahmoudi H., Mahmoudi M., Doustdar O., Jahangiri H., Tsolakis A., Gu S., Wyszynski M. L., 2017, *Biofuels Engineering*, **2**, 11
- Marchione D., et al., 2019, *ACS Earth and Space Chemistry*, **3**, 1915
- Martín-Doménech R., Öberg K. I., Rajappan M., 2020, *ApJ*, **894**, 98
- Martínez-Bach B., Anguera-González A., Pareras G., Rimola A., 2024, *Chemphyschem*
- Massieon C. C., Cutler A. H., Shadman F., 1993, *Industrial & Engineering Chemistry Research*, **32**, 1239
- Mates-Torres E., Rimola A., 2024, *Journal of Applied Crystallography*, **57**, 503
- McGonagle D., Irvine W. M., 1997, *ApJ*, **477**, 711
- McGonagle D., Irvine W. M., Ohishi M., 1994, *ApJ*, **422**, 621
- McKellar A., 1940, *PASP*, **52**, 187
- Minissale M., et al., 2022, *ACS Earth and Space Chemistry*, **6**, 597
- Mugiraneza S., Hallas A. M., 2022, *Commun. Phys.*, **95**, 5
- Nakashima S., Kebukawa Y., Kitadai N., Igisu M., Matsuoka N., 2018, *Life*, **8**
- Oba Y., Tomaru T., Lamberts T., Kouchi A., Watanabe N., 2018, *Nature Astronomy*, **2**, 228
- Olson K. R., Straub K. D., 2016, *Physiology*, **31**, 60
- Pareras G., Cabedo V., McCoustra M., Rimola A., 2023, *A&A*, **680**, A57
- Pareras G., Cabedo V., McCoustra M., Rimola A., 2024, *A&A*, **687**, A230
- Perdew J. P., Ruzsinszky A., Csonka G. I., Vydrov O. A., Scuseria G. E., Constantin L. A., Zhou X., Burke K., 2008, *Phys. Rev. Lett.*, **100**, 136406
- Pereira P. S. S., Macedo L. G. M., Pimentel A. S., 2010, *The Journal of Physical Chemistry A*, **114**, 509
- Perrero J., Enrique-Romero J., Ferrero S., Ceccarelli C., Podio L., Codella C., Rimola A., Ugliengo P., 2022, *ApJ*, **938**, 158
- Perrero J., Beitia-Antero L., Fuente A., Ugliengo P., Rimola A., 2024, *ApJ*, **971**, 36
- Peters S., Semenov D., Hochleitner R., Trapp O., 2023, *Sci. Rep.*, **13**
- Phuong, N. T. et al., 2018, *A&A*, **616**, L5
- Potapov A., Jäger C., Henning T., 2020, *Phys. Rev. Lett.*, **124**, 221103
- Rimola A., Taquet V., Ugliengo P., Balucani N., Ceccarelli C., 2014, *A&A*, **572**, A70
- Rotelli L., Trigo-Rodríguez J. M., Moyano-Camero C. E., Carota E., Botta L., di Mauro E., Saladino R., 2016, *Scientific Reports*, **6**, 38888
- Sanz-Novo M., et al., 2024, *The Astrophysical Journal Letters*, **965**, L26
- Schaefer L., Fegley B., 2010, *Icarus*, **208**, 438
- Schmitt-Kopplin P., et al., 2010, *Proceedings of the National Academy of Science*, **107**, 2763
- Schrader D. L., Zega T. J., 2019, *Geochim. Cosmochim. Acta*, **264**, 165
- Schrader D. L., Davidson J., McCoy T. J., Zega T. J., Russell S. S., Domanik K. J., King A. J., 2021, *Geochim. Cosmochim. Acta*, **303**, 66
- Schulze-Makuch D., Irwin L. N., 2008, *Life in the Universe*, doi:10.1007/978-3-540-76817-3
- Singerling S. A., Brearley A. J., 2018, *Meteorit. Planet. Sci.*, **53**, 2078
- Suttle M. D., Greshake A., King A. J., Schofield P. F., Tomkins A., Russell S. S., 2021, *Geochim. Cosmochim. Acta*, **295**, 286
- Takéuchi Y., Kudoh Y., Sato G., 1985, *Zeitschrift für Kristallographie - Crystalline Materials*, **173**, 119
- Thaddeus P., Kutner M. L., Penzias A. A., Wilson R. W., Jefferts K. B., 1972, *ApJL*, **176**, L73
- VandeVondele J., Krack M., Mohamed F., Parrinello M., Chassaing T., Hutter J., 2005, *Computer Physics Communications*, **167**, 103
- Walde P., 2005, Springer, Berlin, Germany, doi:https://doi.org/10.1007/b105128
- Weisberg M. K., McCoy T. J., Krot A. N., 2006, *Systematics and Evaluation of Meteorite Classification*, p. 19
- Woo K., Hong J. and Choi S., Lee H., Ahn J., Kim C. S., Lee S. W., 2004, *Chem. Mater.*, **16**, 2814
- Wordsworth R. D., 2016, *Earth and Planetary Science Letters*, **447**, 103
- Zahnle K., Schaefer L., Fegley B., 2010, *Cold Spring Harbor Perspectives in Biology*
- Zolensky M. E., Thomas K. L., 1995, *Geochim. Cosmochim. Acta*, **59**, 4707
- Zolensky M. E., Weisberg M. K., Buchanan P. C., Mittlefehldt D. W., 1996, *Meteorit. Planet. Sci.*, **31**, 518
- Zolensky M. E., Krot A. N., Benedix G., 2008, *Reviews in Mineralogy and Geochemistry*, **68**, 429

This paper has been typeset from a $\text{\TeX}/\text{\LaTeX}$ file prepared by the author.